Scientific Reports

https://doi.org/10.1038/s41598-026-43892-z

Article in Press

Multifractal evolution of shale fracture and pore structures under uniaxial compression

Received: 24 December 2025

Accepted: 6 March 2026

Published online: 21 March 2026

Cite this article as: Wang Z., Sun J., Wen H. *et al.* Multifractal evolution of shale fracture and pore structures under uniaxial compression. *Sci Rep* (2026). https://doi.org/10.1038/s41598-026-43892-z

Ziqi Wang, Jianmeng Sun, Haiou Wen, Weiliang Pan, Xiaojuan Sun & Honlin Gao

Multifractal Evolution of Shale Fracture and Pore Structures under Uniaxial Compression

Ziqi Wang[1*], Jianmeng Sun[1], Haiou Wen[2], Weiliang Pan[1], Xiaojuan Sun[1], Honlin Gao[1]

(1. School of Geosciences, China University of Petroleum (East China), Qingdao 266580, China;

2. College of Mining, Liaoning Technical University, Fuxin, 123000, China)

*Corresponding author: Ziqi Wang, E-mail: wangziqi9604@163.com.

Abstract: The evolution of fracture-pore structures critically controls the mechanical stability and permeability of shale reservoirs. To clarify their coupled behavior during stress-induced failure, we investigate the multifractal evolution of fractures and pores in shale under uniaxial compression using digital rock reconstruction and discrete element modeling. The proposed fracture-damage framework reproduces fracture nucleation, propagation, and coalescence, and reveals a strong correspondence between energy conversion and damage development. Multifractal analyses show that pore heterogeneity primarily governs the fractal characteristics at the early loading stage, whereas fracture growth becomes increasingly dominant after peak stress; meanwhile, the multifractal parameters of fractures and pores evolve in broadly consistent trends. Together with the simulated porosity and permeability responses, these fractal descriptors capture the progressive reorganization of flow pathways during loading. Overall, this work provides a quantitative structure-property link between fracture activity, pore complexity, and transport evolution in shale, offering mechanistic insights for reservoir failure interpretation and stability evaluation.

Keywords: DEM; digital rock; pore structure; fracture evolution; multifractal analysis

1. Introduction

As deep resource exploitation and underground construction move into more challenging settings, the mechanical stability of rock masses has become a primary constraint on engineering safety and energy recovery efficiency[1-3]. Under loading, rock microstructure evolves in a strongly nonlinear manner, involving crack initiation and growth, pore restructuring, and changes in pore connectivity. These microscopic processes ultimately control the macroscopic mechanical response. In oil and gas reservoirs, they also regulate flow pathways and production stability, making them important for both fundamental understanding and engineering practice[4-6]. Despite this relevance, the coupled evolution between fracture activity and pore-structure change is not yet well resolved. Clarifying how these two processes correlate and co-develop during loading is therefore essential for revealing failure micromechanisms and for more reliable assessment of reservoir stability.

Over the past decade, fracture growth and pore-structure evolution in rocks under loading have been intensively investigated using experiments, theory, and numerical modeling, improving our understanding of deformation and failure mechanisms across scales. X-ray CT has become a key tool for tracking micro damage development during loading, and many studies describe a staged process comprising pore compaction, crack nucleation, stable growth of dominant cracks, and rapid crack coalescence leading to failure[7-9]. Discrete element simulations have further reproduced crack initiation and interaction under compression, highlighting pore geometry as a major control on failure mode and mechanical response[10,11]. Related work has also linked porosity evolution to changes in strength and stiffness[12-14]. When CT-derived pore networks are integrated with numerical models, the three-dimensional pore architecture emerges as a key factor governing global stability[15,16].

Several studies have also approached fracture activity from a signal-response viewpoint. Changes in electrical or charge-related signals that accompany crack initiation and growth have been shown to track the evolving internal fracture state of rock masses[17-20]. In addition, Yin et al. reported that stress-drop events correlate with bursts of signal energy release, providing a basis for interpreting the timing and intermittency of crack activity[21].

More recently, growing evidence suggests that physical signals emitted during rock failure are nonlinearly linked to internal structure and often exhibit fractal or multifractal characteristics. Fractal features have been identified in surface potential, acoustic emission (AE), and electromagnetic radiation (EMR) signals. For example, Niu et al. showed that the multifractal dimensions of EMR signals vary dynamically during coal-rock deformation and fracture and have been used for dynamic-disaster forecasting[22]. Likewise, Liu et al. used multifractal analysis of AE signals under different loading levels to indicate that changes in fractal parameters reflect fluctuations in failure mechanisms and energy-release behavior[23].

Beyond signal-based studies, Gu et al. demonstrated that fractal geometry is an effective mathematical tool for characterizing rock microstructures. Traditional single-fractal dimensions have been utilized to analyze the structural complexity of digital images and fracture surfaces, providing a parametric representation of morphology[24]. In addition, Li et al. employed a multifractal approach to investigate the complexity of rock pore structures, and they further explored the intrinsic relationship between pore characteristics and mechanical properties through numerical simulations[25]. Furthermore, recent advances have integrated fractal theory with mechanical characterization to better capture the lamination effects and adsorption behaviors in complex shale reservoirs[26,27].

Although substantial progress has been made in understanding fracture evolution, pore structure variation, and their energy characteristics during rock loading and failure, systematic investigations into the intrinsic relationship between fracture-related signals and the multifractal properties of pore structures remain limited. Owing to the complex pore architecture, pronounced anisotropy, and high stress sensitivity of shale, its microscale structural evolution strongly affects reservoir stability and fluid migration. Therefore, this study employs a discrete element method (DEM) based on digital rock models to systematically analyze the multifractal evolution of shale fracture signals and pore structures under uniaxial compression. The results reveal the corresponding relationships and synergistic evolution patterns between these two aspects during loading. This research enhances the

understanding of shale microfracturing mechanisms and provides a theoretical basis for evaluating reservoir stability and quantitatively characterizing pore structure complexity.

2. Methodology

Shale cores were taken from the Fengcheng Formation in Well MaYe1 (Ma Bei Oilfield) at depths of 3484.62-3500.12 m. The operating company supplied the samples under a formal technical service project. The cores were collected during routine geological/engineering operations, and their use in academic research was authorized through the associated service agreement; therefore, no additional collection permit was required. The digital-rock modeling procedure is described below:

2.1 Micro-CT Scanning and Image Processing

Cylindrical shale specimens (4 mm in diameter) were prepared from the core by wire cutting. After the end faces were flattened and polished, the samples were scanned by micro-CT, producing 1,220 consecutive grayscale slices (0-255). Dark voxels (near 0) represent pores and fractures, bright voxels (near 255) indicate high-density minerals, and intermediate gray corresponds to the shale matrix.

The CT image stacks were batch processed in Avizo. Median filtering was used to suppress noise and imaging artifacts, followed by contrast enhancement and threshold-based segmentation to extract the pore phase. Because the micro-CT voxel size is on the micrometer scale, the analysis mainly captures imaging-resolved micrometer pores and fractures and does not include the dominant nanoscale porosity in shale. Accordingly, the porosity reported here represents the structure of the resolvable pore-fracture network rather than the total pore space. For comparison, four samples spanning different porosity levels were selected, and their 3D pore architectures are shown in Figure 1.

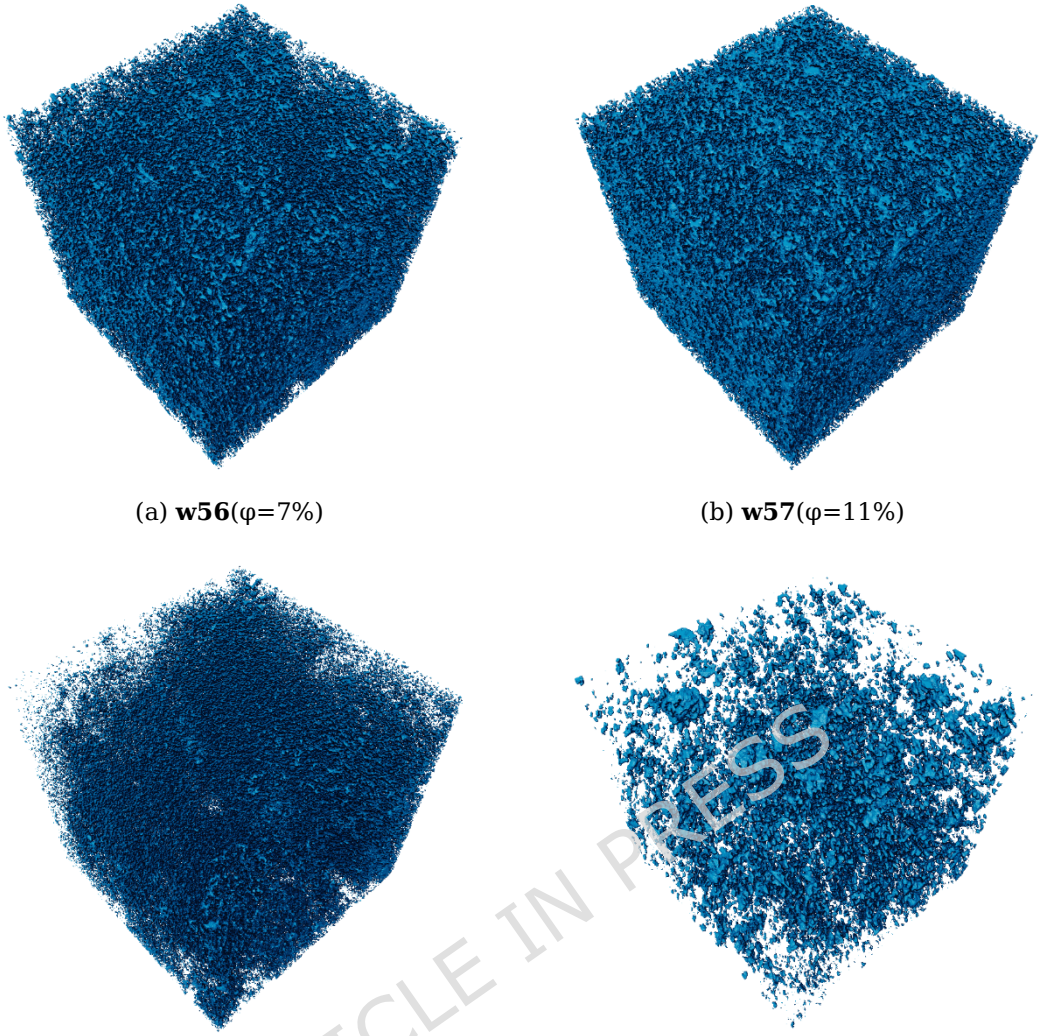

(a) **w56**(φ=7%) (b) **w57**(φ=11%)

(c) **w60**(φ=3%) (d) **w62**(φ=2%)

Figure.1 Three-dimensional pore structure of rock core

2.2 Three-dimensional reconstruction of digital rocks and processing of simulation results

Figure 2 summarizes the workflow for 3D digital-rock reconstruction and simulation post-processing. The segmented CT volume was exported as a RAW file and imported into MATLAB, where a custom script extracted pore coordinates and saved them as an Excel table. A cubic PFC model with the same voxel resolution was then created. Pore data were read in via the built-in Python interface, and the corresponding 3D DEM geometry was generated using FISH to match the CT-derived structure. After simulation, outputs were written to TXT files, converted in MATLAB to 3D TIFF stacks, and finally processed and visualized in Avizo.

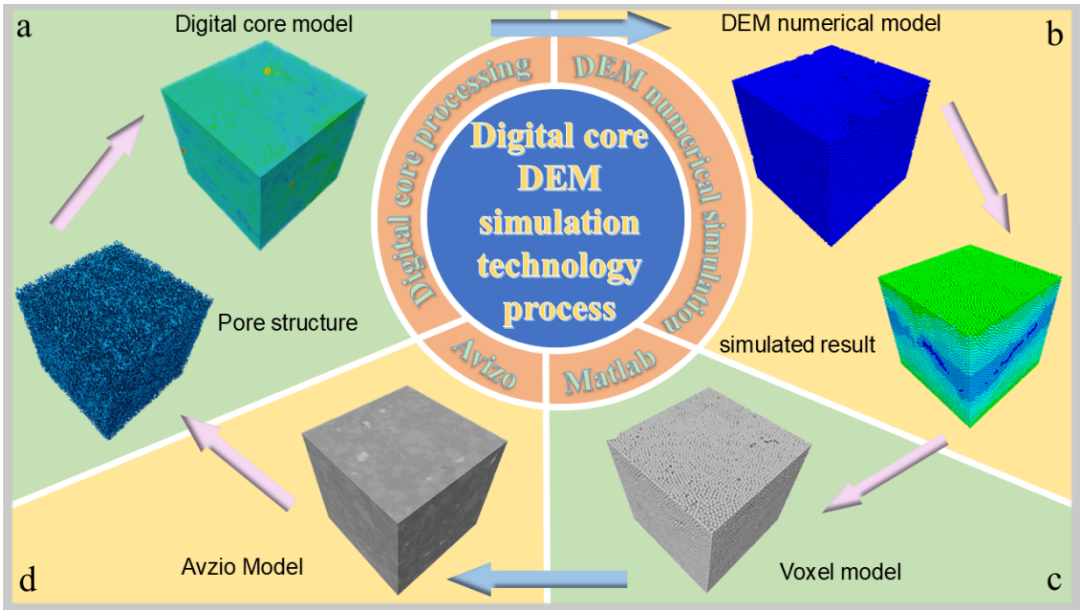

Figure.2 Workflow of CT-based digital rock analysis combined with discrete element simulation

Figure 3 outlines the specimen preparation and loading scheme. A random particle packing was first created using servo control, with boundary stress adjusted incrementally until isotropic equilibrium was achieved. Interparticle bonds were then assigned to form the rock-like microstructure. Two contact laws are compared: the linear model, which includes only normal and shear elasticity, and the parallel-bond model, which further introduces bending stiffness and bond moments to better capture brittle response and shear-related failure.

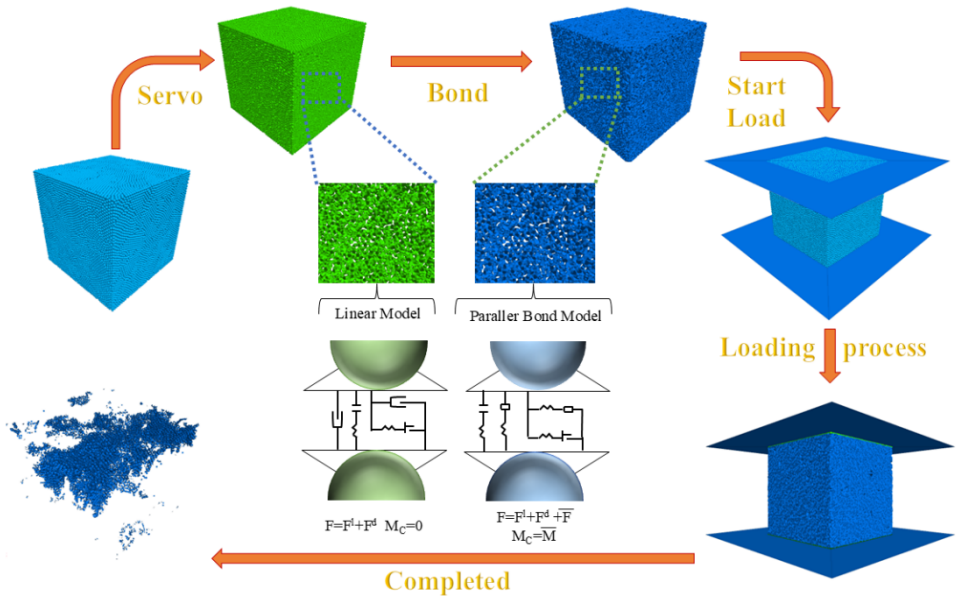

Figure.3 DEM computation workflow

Loading was subsequently activated at the boundaries to perform uniaxial compression. The top and bottom platens were driven at a constant velocity, and damage evolved as microcracks initiated, grew, and coalesced into a macroscopic failure pattern at the end of loading. The simulation thus reproduces the full stress-strain response, from the elastic regime through peak strength and into the post-peak stage.

2.3 Multifractal theory

During the evolution of shale fractures or pores, their multifractal characteristics can be quantitatively characterized using the Box Dimension Method. First, the digital rock or signal sequence $x(i)$ is divided into e subintervals (or small boxes) at scale N[28,29]

Let the probability distribution function of the average signal amplitude in the i-th small box be denoted as $p_i(e)$. Then its expression is:

$$P_i(e) = \frac{S_i(e)}{\sum_{i=1}^{N} S_i(e)} \tag{1}$$

Here, $s_i(e)$ is the sum of signal amplitudes within the i-th subbox, with the denominator being the total sum of signal amplitudes across the entire sequence.

Define distribution function $c_q(e)$ as:

$$c_q(e) = \sum_{i=1}^{N} P_i(e)^q \sim e^{t(q)} \tag{2}$$

Here, q is the weighting factor, and $t(q)$ is the mass index. Different values of q reflect the influence of signals with varying amplitudes in the overall distribution: when $q < 1$, small-amplitude signals dominate; when $q > 1$, large-amplitude signals dominate.

To further characterize Multifractal features, the generalized dimension $D(q)$ is introduced, defined as follows:

$$D(q)=\begin{cases}\dfrac{1}{q-1}\lim\limits_{\varepsilon\to 0}\dfrac{\sum_{i=1}^{N}P_i(\varepsilon)^q\ln P_i(\varepsilon)}{\ln\varepsilon} & (q\neq 1)\\ \lim\limits_{\varepsilon\to 0}\dfrac{\sum_{i=1}^{N}P_i(\varepsilon)\ln P_i(\varepsilon)}{\ln\varepsilon} & (q=1)\end{cases} \tag{3}$$

To further characterize multifractal features, the generalized dimension $D(q)$ is introduced, defined as follows: By calculating $D(q)$ for different q values, the generalized dimension curve $D(q)-q$ is obtained. A larger variation amplitude indicates stronger signal volatility in the system and more pronounced multifractal characteristics.

$$\alpha=\frac{d(t(q))}{dq}=\frac{d}{dq}\left(\lim_{\varepsilon\to 0}\frac{\ln c_q(\varepsilon)}{\ln\varepsilon}\right) \tag{4}$$

Furthermore, using the Legendre transformation, the singular spectral function can be derived from the $D(q)-q$ relations.

$$\alpha=\frac{dt(q)}{dq},\quad f(\alpha)=q\alpha-t(q) \tag{5}$$

Here, α is the singular strength index, and $f(\alpha)$ is the multifractal spectrum. The morphology of the function $f(\alpha)-\alpha$ reflects the non-uniform distribution characteristics of cracks or pore structures across different scales, with its spectral width serving as a measure of the system's complexity and fractal degree.

2.3 Rock mechanics tests and model parameters

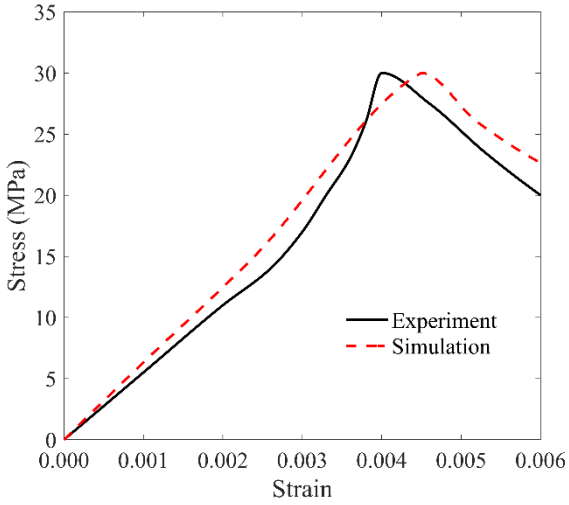

Figure.4 Uniaxial compression stress-strain curve

Uniaxial compression tests were performed on shale cores taken from the same stratigraphic interval in the study area, giving a peak strength of 33 MPa and an elastic modulus of 8 GPa. A 3D DEM specimen with the same size as the digital rock (1 mm × 1 mm × 1 mm) was then built in PFC using the parallel-bond model, and uniaxial loading was imposed by rigid platens to reproduce the laboratory loading path.Because DEM micro-contact properties are not directly measurable, they were calibrated against the experimental response. Parameters were tuned iteratively until the simulated stress-strain curve matched the test data in both peak strength and modulus (Fig. 4). The final set is: effective modulus 16.5 GPa, bond modulus 16.5 GPa, normal-to-tangential stiffness ratio 1.50, bonded normal-to-tangential stiffness ratio 1.50, cohesion 1.26 MPa, and friction angle 45°.

3. Compression simulation results for digital rocks

Figure 5 compares stress transfer in shale models with different porosities. As porosity increases, the load-transfer network evolves from relatively continuous and concentrated force-chain pathways to more dispersed and discontinuous patterns. Low-porosity specimens form well-connected force chains aligned with the loading direction, sustaining higher bearing capacity and structural integrity. In contrast, higher porosity disrupts these chains, promotes stress localization around pores, and increases instability.

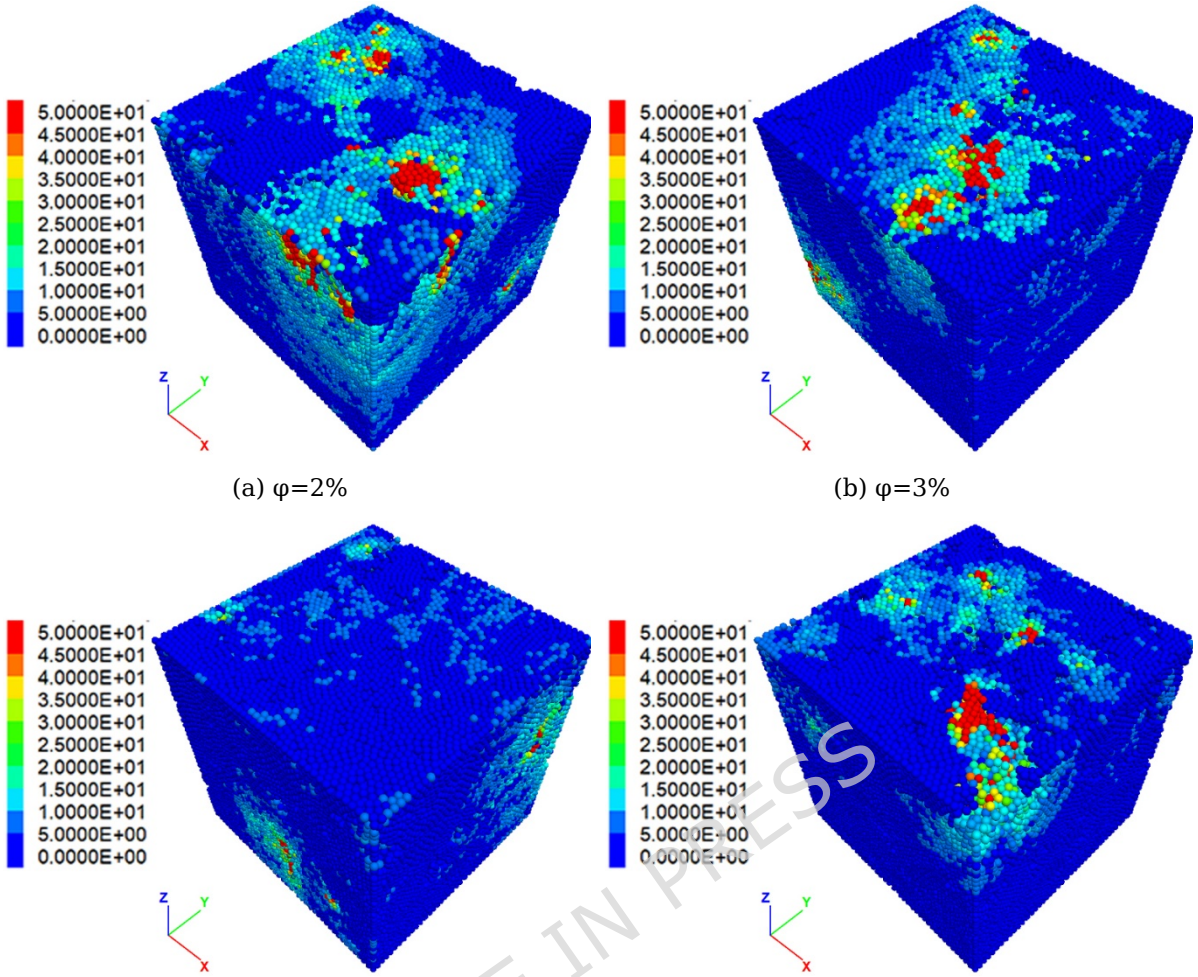

(a) φ=2% (b) φ=3%

(c) φ=7% (d) φ=11%

Figure 5 Contact-force maps (different porosities)

These observations suggest that pore architecture controls both the continuity of stress transmission and the preferred sites of crack initiation and growth, thereby facilitating fracture-network development at higher porosity. Moreover, the contact-force evolution provides a mechanical basis for linking microscale damage processes to the subsequent multifractal characterization of fracture-pore structures.

Figure 6 illustrates that porosity strongly influences the displacement field and failure pattern under uniaxial loading. With increasing porosity, the granular framework is less constrained and deformation becomes more heterogeneous. In low-porosity specimens, displacement localizes into narrow, band-like zones roughly aligned with the principal loading direction, indicating shear-dominated localization while the overall framework remains relatively intact. In contrast, high-porosity specimens exhibit a more diffuse displacement field, accompanied by stronger local

fragmentation and more frequent through-going fractures.

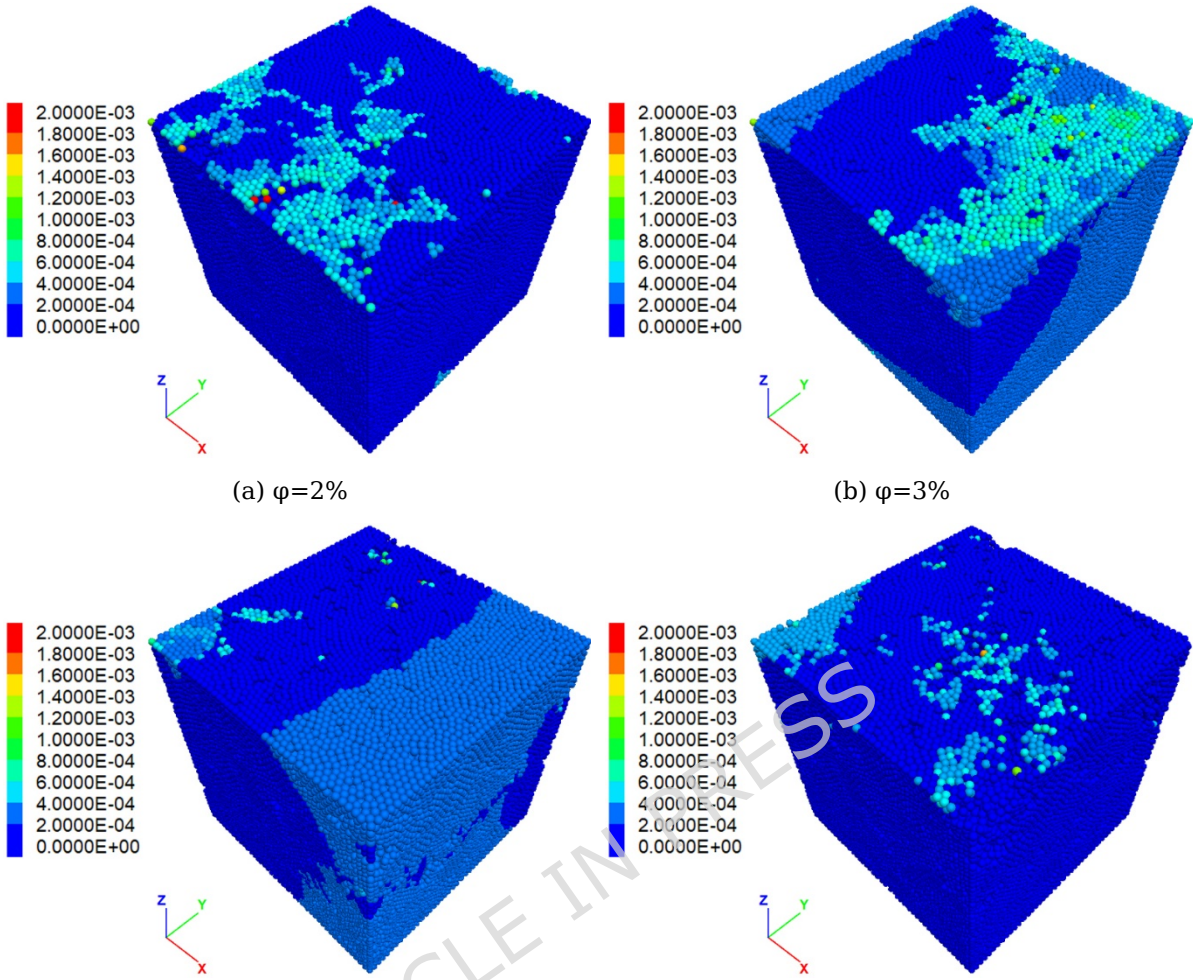

(a) φ=2% (b) φ=3%

(c) φ=7% (d) φ=11%

Figure.6 Displacement maps (different porosities)

As porosity increases, the load-bearing skeleton becomes less continuous and stress/displacement transfer shifts from coherent force-chain pathways to more intermittent routes. This reduces the dominance of a single localization band and promotes more distributed damage. Consequently, low-porosity shale sustains higher loads through a more connected bearing framework, whereas high-porosity shale shows broader strain partitioning, earlier coalescence of damaged zones, and a corresponding reduction in macroscopic load-bearing capacity.

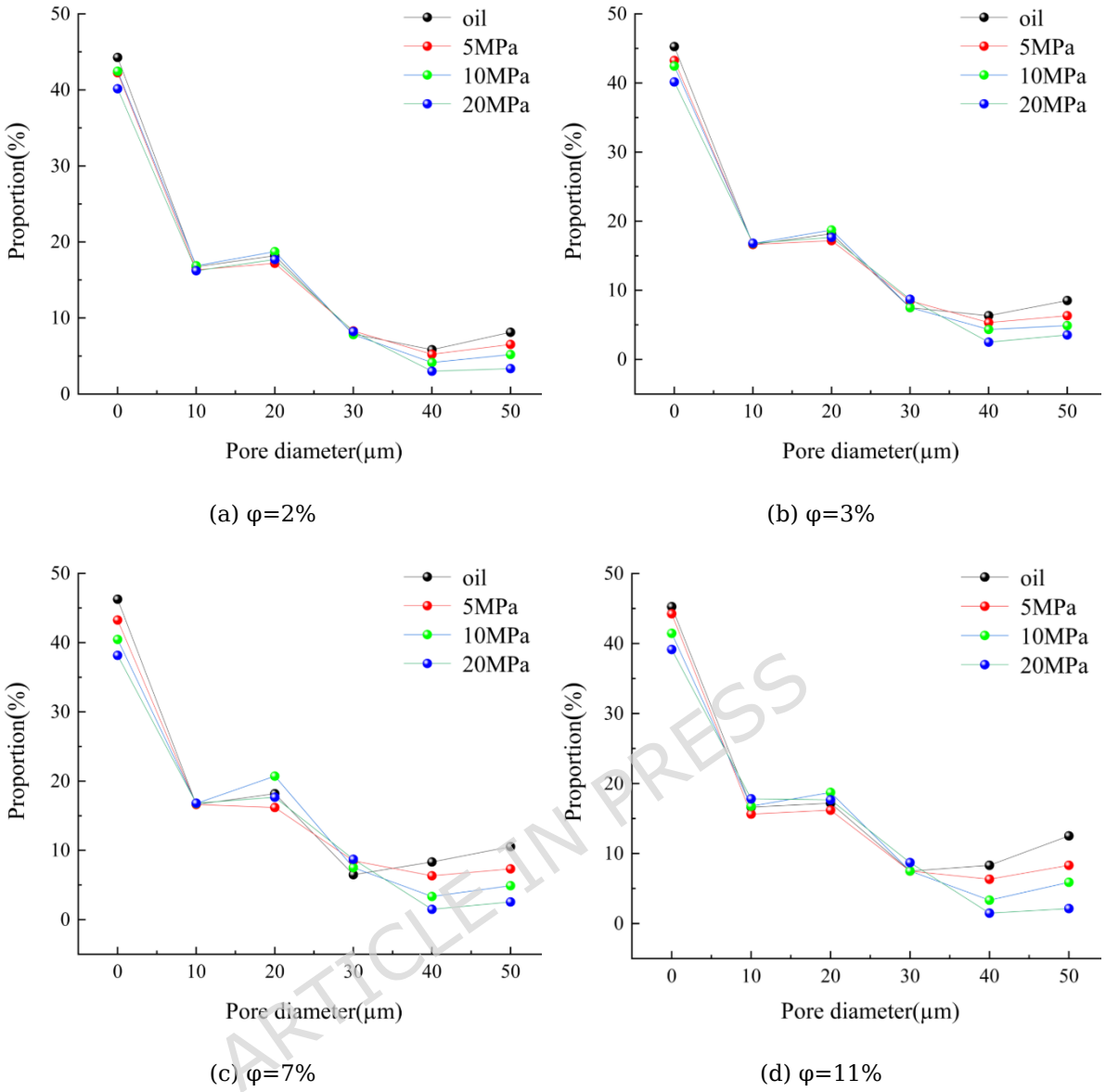

Figure.7 Pore size distribution in digital rocks with different porosities

Figure 7 shows the pore-size distribution of shale samples with different initial porosities under uniaxial compression. With increasing load, the pore system is progressively compacted and reorganized: the fraction of micropores (<10 μm) decreases slightly, pores in the 10–30 μm range fluctuate, and the macropore fraction (40–50 μm) decreases markedly, indicating gradual closure or constraint of large pores under stress. For initial porosities of 2%, 3%, 7%, and 11%, the reduction in the 40–50 μm pore fraction is 4%, 4.5%, 6%, and 7%, respectively, suggesting a stronger large-pore evolution in higher-porosity samples. Overall, loading narrows the pore-size distribution and reduces the proportion of large pores, reflecting a

transition from a relatively open to a more compact pore structure with increased heterogeneity.

As shown in Figure 8, both the peak strength (σ_p) and elastic modulus (E) generally decrease with increasing porosity over φ = 2–11% (2, 3, 4, 6, 7, 8, 10, and 11%). Overall, σ_p decreases from ~23 MPa to ~14 MPa, and E decreases from ~17 GPa to ~14.5 GPa, indicating that increasing porosity weakens the load-bearing capacity and stiffness of shale. Meanwhile, mild non-monotonic variations are observed at intermediate porosities (e.g., slight increases around 3% and 6%, and a weak plateau-like feature around 7-8%), suggesting that porosity provides a first-order but not exclusive control on the mechanical response.

Mechanistically, higher porosity increases both the number and average size of pores, thereby reducing the effective fraction of the load-bearing solid matrix. Because pores contribute negligibly to compressive resistance, stresses are redistributed and become increasingly concentrated within the remaining matrix, promoting microcrack initiation and coalescence. As loading proceeds, these localized high-stress regions expand and connect, accelerating matrix damage and stiffness degradation, which ultimately manifests as lower σ_p and E.

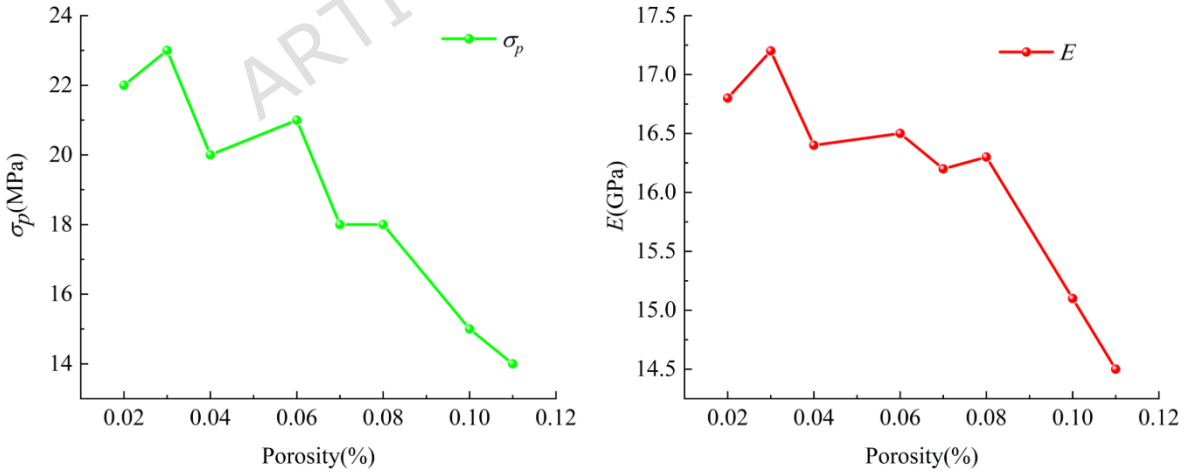

(a) Peak intensity (b) Modulus of elasticity

Figure.8 Peak strength and elastic modulus of digital rocks with different porosities

It is noteworthy that porosity is not the only controlling factor. The modest fluctuations superimposed on the overall downward trend imply that the mechanical response is also influenced by pore-structure attributes, including pore-size

distribution, pore morphology, and connectivity. A relatively uniform and poorly connected pore network may delay stress localization and microcrack propagation, thereby partially preserving stiffness and strength. Therefore, porosity provides a primary indicator of mechanical weakening, while intrinsic pore-structure characteristics help explain the secondary variability among different porosity levels.

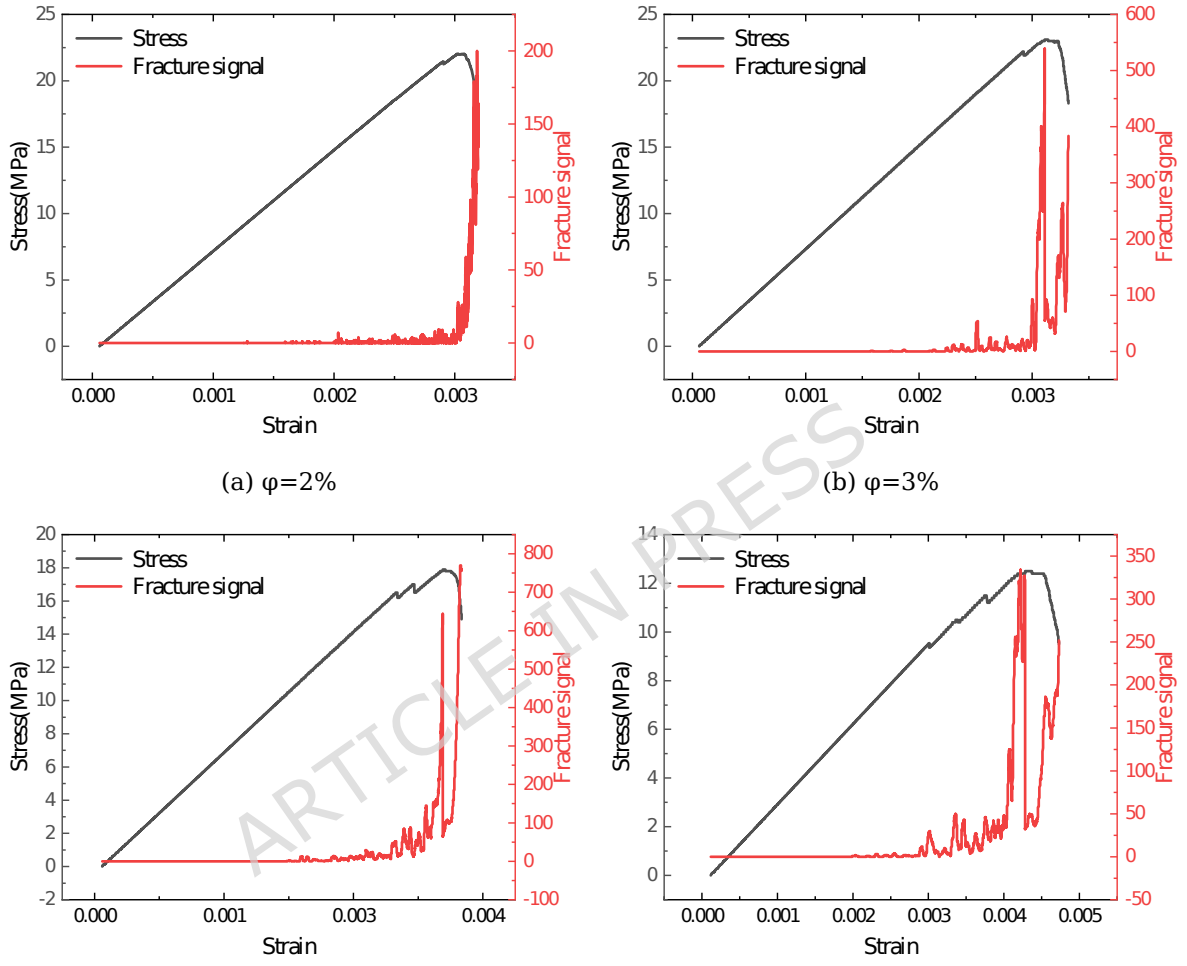

Figure.9 Stress-strain and crack signal curve

As shown in Figure 9, shale samples with different porosities exhibit distinct stress–strain responses and fracture-signal evolutions during uniaxial loading. In the early stage, fracture activity is limited, the fracture signal remains low, and the stress–strain curve is approximately linear. With continued loading, microcracks initiate and grow, leading to intermittent increases in fracture-signal intensity. Near the peak stress and into the post-peak regime, the fracture signal rises sharply and shows high-frequency fluctuations, indicating rapid crack propagation and

coalescence that culminate in macroscopic failure.

These results indicate that the fracture signal effectively reflects the timing and intensity of damage evolution and closely tracks key stages of the stress–strain response. Combined with the contact-force, displacement, and pore-size analyses, the higher-porosity samples show a weakened load-bearing skeleton, which promotes earlier crack initiation and more unstable crack growth. Accordingly, their fracture signals display more frequent pre-peak fluctuations and stronger post-peak energy release.

Notably, fracture signals exhibit multiscale, intermittent, and non-stationary behavior rather than a simple monotonic trend, and the fluctuation patterns vary across porosities, reflecting the influence of internal structural complexity. Therefore, single-scale descriptors are insufficient to capture the temporal organization of fracture activity. To quantify these complex features and enable a consistent comparison with the geometric characteristics of the pore system, multifractal analysis is introduced in the following section.

4. Multifractal analysis of fracture-pore structures

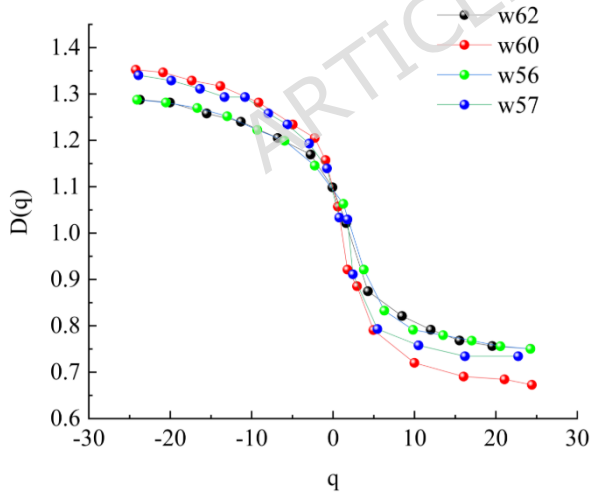

(a) early(fracture signal)

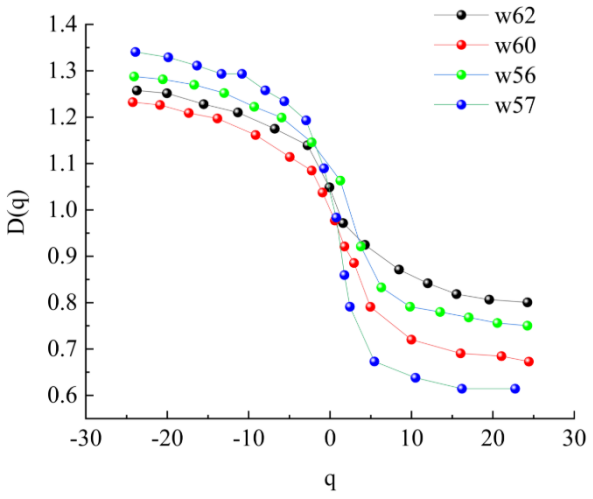

(b) early(pore structure)

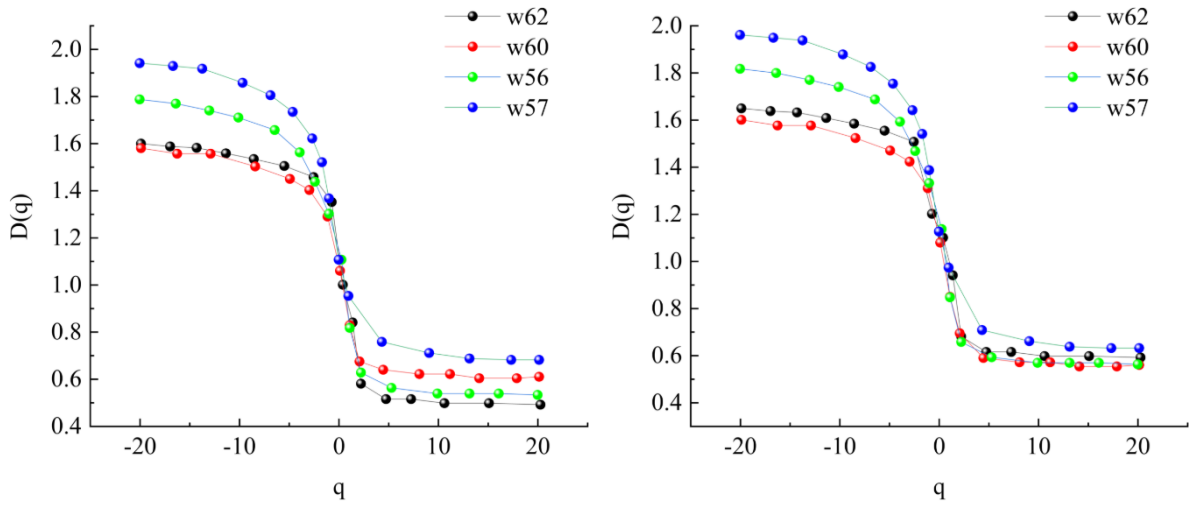

(c) lastly(fracture signal)

(d) lastly(pore structure)

Figure.10 Generalized dimension distributions of pore structures and fracture signals

As shown in Figure 10, both the fracture signals and pore structures exhibit clear multifractal characteristics across different loading stages. For both datasets, the generalized dimension $D(q)$ decreases with increasing q, indicating a non-uniform, scale-dependent organization and pronounced heterogeneity in the fracture–pore system[30]

At the early loading stage (Figures 10a and 10b), fractures are not yet well developed and the fracture-related $D(q)$ curve shows only minor variations, suggesting limited fracture activity. In contrast, the pore-structure $D(q)$ distribution is more dispersed, implying that the pore space already possesses appreciable multiscale complexity prior to loading, and the heterogeneity is dominated by the pre-existing pore architecture.

With continued loading (Figures 10c and 10d), the multifractal features of fracture signals become more pronounced. In particular, $D(q)$ increases in the low-q range, which emphasizes the contribution of large-magnitude events, indicating intensified energetic fracture activity and enhanced heterogeneity[23]. Meanwhile, the pore-structure $D(q)$ curve also shows larger variation, and the generalized-dimension characteristics of fracture signals and pore structures tend to converge at later stages, supporting their coupled evolution during microfracturing and pore-structure modification.

As shown in Figure 11, both the fracture signals and pore structures exhibit pronounced multifractal spectra across loading stages. The spectral width $\Delta\alpha$ characterizes the degree of heterogeneity, the branch-height difference Δf reflects the relative dominance of large- versus small-magnitude events, and the peak position α_0 represents the characteristic singularity strength of the system.

At the early loading stage, the multifractal spectrum of the fracture signal is relatively narrow, with a slightly elevated right branch ($\Delta f > 0$), indicating that fracture activity is mainly composed of small-magnitude, spatially dispersed events and the system remains comparatively stable. The pore-structure spectrum is also relatively concentrated, but with a slightly larger $\Delta\alpha$ than the fracture signal, suggesting that the pore space already exhibits inherent heterogeneity prior to loading. Meanwhile, α_0 falls within a moderate singularity range and the spectrum is nearly symmetric or weakly right-skewed, implying that the system response at this stage is dominated by the pre-existing pore architecture.

With continued loading, the fracture-spectrum broadens markedly (increasing $\Delta\alpha$), accompanied by a left-branch enhancement ($\Delta f < 0$) and a shift of α_0 toward smaller α. These changes indicate an increasing contribution of large-magnitude fracture events, consistent with rapid crack propagation and coalescence. The pore-structure spectrum shows a more moderate broadening and a weaker leftward shift, implying pore reorganization under stress but with a comparatively smoother response than the fracture system.

Overall, both spectra evolve from slightly right-skewed to left-skewed profiles (Δf changes from positive to negative) together with spectrum broadening, supporting the coupled evolution of fracture activity and pore-structure modification during loading. Notably, the fracture signal exhibits stronger multifractal variability, highlighting its higher sensitivity to stress perturbations, whereas the pore structure reflects the progressive increase in overall structural complexity.

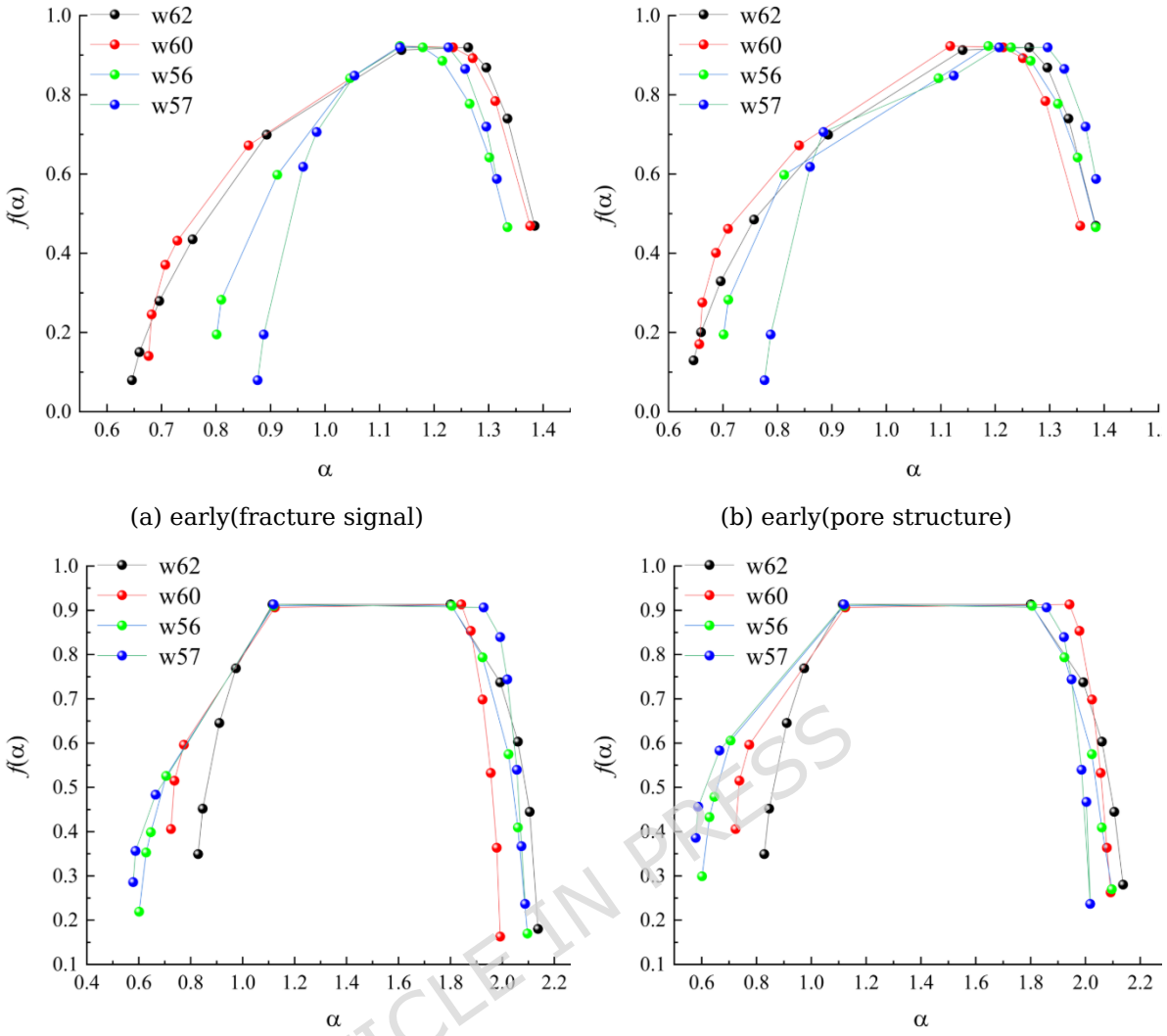

(a) early(fracture signal)

(b) early(pore structure)

(c) lastly(fracture signal)

(d) lastly(pore structure)

Figure.11 Multifractal spectra of pore structures and fracture signals

5. Multifractal characteristic analysis of crack-pore structure damage evolution

5.1 Energy-based characterization of crack damage evolution

Figure 12 illustrates the progressive damage evolution of shale under uniaxial loading. With increasing stress, the internal pores of the specimen first experience compaction and deformation. Subsequently, microcracks initiate at zones of localized stress concentration and continue to propagate and coalesce, eventually forming a through-going fracture network across the entire sample. This figure intuitively demonstrates the failure evolution of shale—from an initially intact structure to a fully fractured state.

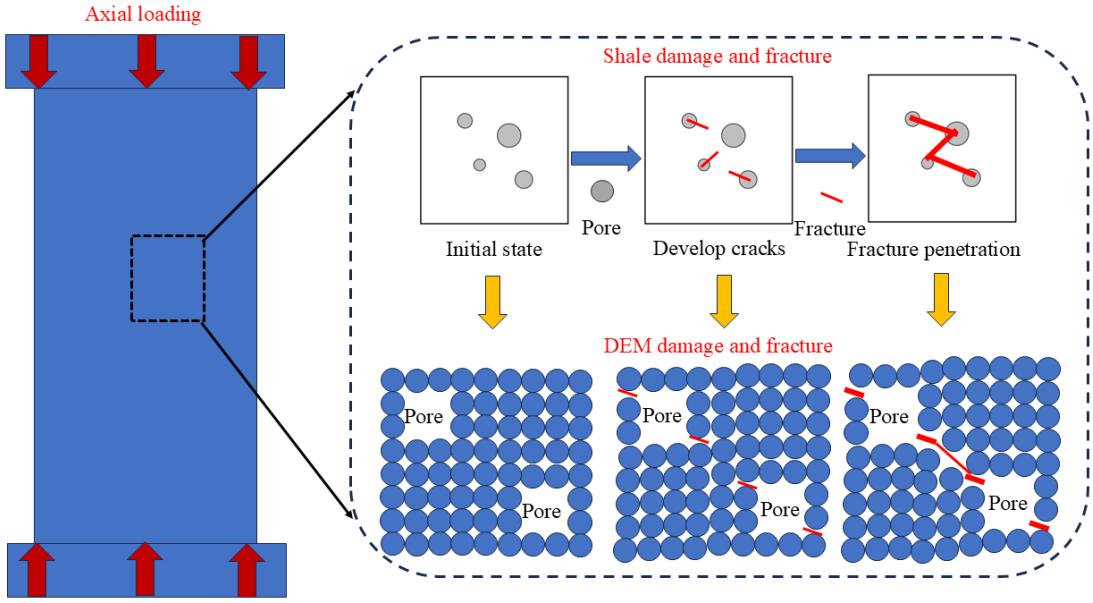

Figure.12 Schematic illustration of core damage and failure under uniaxial compression

As shown in Figure 13, the curve exhibits a brief stress drop from S_1 to S_2 before the peak, followed by a continued rise to the global peak. his phenomenon indicates that before overall failure, localized crack propagation in the shale induces a transient release of stored energy, while the system still retains its load-bearing capacity. This process reflects the staged transition among energy storage, dissipation, and release, providing key insight into the progressive failure mechanism of shale[31-33].

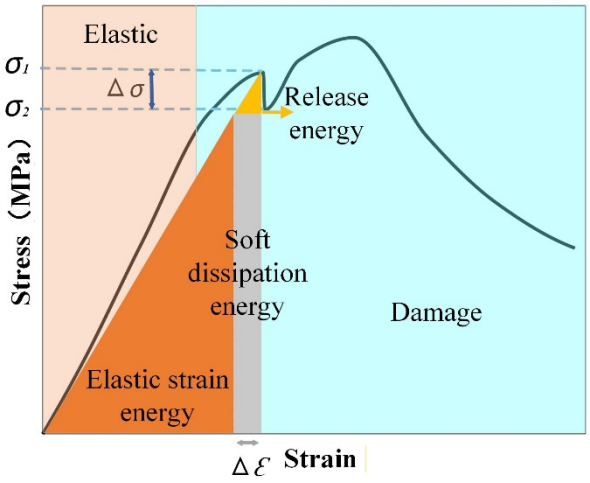

Figure.13 Schematic diagram of energy conversion during rock mass fracturing process

The overall energy balance during the deformation and fracturing process of shale can be expressed as follows:

$$U_{\text{total}} = U_s + U_{\text{dr}} \tag{6}$$

Among them:

U_s：Elastic energy

U_{dr}：Total energy dissipated and released

Suppose that during a sudden event, the stress in a rock mass decreases from s_1 to s_2, corresponding to a strain of Δe. The energy conversion during this process can be expressed as:

Release Energy:

$$U_{\text{rel}} = \frac{1}{2}(s_1 - s_2)\Delta e = \frac{1}{2}\Delta s \Delta e \tag{7}$$

Dissipated energy:

$$U_{\text{diss}} = s_2 \Delta e \tag{8}$$

Total energy dissipated and released:

$$U_{\text{dr}} = U_{\text{diss}} + U_{\text{rel}} \tag{9}$$

Substituting equations (7) and (8) into (9) yields:

$$U_{\text{dr}} = \frac{1}{2}(s_1 + s_2)\Delta e \tag{10}$$

During the loading and fracturing process of shale, energy release is closely associated with crack initiation. The formation of cracks essentially represents the dissipation of internal energy and the degradation of the rock's structural integrity. To further describe the damage evolution induced by this energy release from a geometrical perspective, variations in the number of cracks can be used as a quantitative measure. If Q_m denotes the total number of cracks within the cross-sectional area A, the crack generation rate per unit area can then be defined as:

$$i_q = \frac{Q_m}{A} \tag{11}$$

The damage factor D characterizes the internal failure extent of rock mass and can be normalized by the cumulative crack length. If the corresponding damaged area is denoted as A_d, the damage factor D can be expressed as:

$$D = \frac{A_d}{A} \tag{12}$$

When the cross-sectional failure area reaches A_d, the cumulative number of cracks can be expressed as:

$$Q_d = A_d \times i_q \tag{13}$$

Substitute Equation 11 into Equation 13:

$$Q_d = \frac{A_d \times Q_m}{A} \tag{14}$$

From (12) to (14), it can be seen that:

$$D = \frac{A_d}{A} = \frac{Q_d}{Q_m} \tag{15}$$

For uniaxial loading, the damage-strain relationship can be expressed as:

$$\frac{dA_d}{A} = dD = f(e)\,de \tag{16}$$

When damage occurs, if the cross-sectional strain increases to e, then

$$D = \frac{A_d}{A} = \int_0^e f(e)\,de \tag{17}$$

$f(e)$ is a continuous function reflecting volumetric unit damage, assuming the strength of micro-elements in the medium follows a Weber distribution function.

$$f(e) = \frac{m}{e_0}\left(\frac{e}{e_0}\right)^{m-1} \exp\left[-\left(\frac{e}{e_0}\right)^m\right] \tag{18}$$

Substituting equation (18) into equation (17) yields:

$$D = 1 - \exp\left[-\left(\frac{e}{e_0}\right)^m\right] \tag{19}$$

The crack increment is:

$$dA_d = A\frac{m}{e_0}e^{m-1}\exp\left[-\left(\frac{e}{e_0}\right)^m\right]de \tag{20}$$

The cumulative crack length is:

$$A_d = A\left\{1-\exp\left[-\left(\frac{e}{e_0}\right)^m\right]\right\} \tag{21}$$

Considering that specimens often fail incompletely during actual loading, a normalization process must be introduced, yielding[34,35]:

$$\frac{D}{D_u} = \frac{Q_d}{Q_m} \tag{22}$$

Where D_u is the critical damage factor, and Q_m is the corresponding accumulated crack signal.

By further incorporating the ultimate strength from the stress-strain relationship, D_u can be expressed as:

$$D_u = 1-\frac{s_r}{s_c} \tag{23}$$

The final expression for the corrected damage factor is obtained as follows:

$$D_r = \left(1-\frac{s_r}{s_c}\right)\times\frac{A_d}{A} = \left(1-\frac{s_r}{s_c}\right)\times\frac{Q_d}{Q_m} \tag{24}$$

According to damage mechanics, it can be derived that:

$$s = Ee(1-D_r) = Ee\left(1-\frac{s_r}{s_c}\right)\exp\left[-\left(\frac{e}{e_0}\right)^m\right] \tag{25}$$

Or written as:

$$s = Ee(1-D_r) = Ee\left(1-\frac{s_r}{s_c}\right)\exp\left(1-\frac{A}{A_d}\right) \tag{26}$$

It can therefore be concluded that fracture signals are strongly correlated with rock damage, and that the development of damage exerts a significant influence on the stress state during the rock loading process.

After establishing the theoretical framework of the damage factor, a quantitative coupling is introduced between the directly released energy density per unit volume

w_{dr}, as derived from the energy release theory, and the damage factor D_t to further elucidate their intrinsic relationship. Considering the critical role of energy release in crack propagation, it is assumed that the damage factor is directly proportional to the energy release density, expressed as:

$$w_{dr} = k \times D_t \tag{27}$$

Here, k is a proportional coefficient that quantifies the sensitivity of shale damage to the release of unit energy. This expression highlights the controlling influence of directly released energy on the dominant mechanisms of fracture evolution.

A unified relationship can thus be further derived as follows:

$$\frac{1}{2}(s_1 + s_2) \times De = k \times \left(1 - \frac{s_r}{s_c}\right) \times \frac{Q_d}{Q_m} \tag{28}$$

The computational results based on the modified damage model are presented in Figure 14. During uniaxial compression, the stress, damage factor, instantaneous dissipated energy density increment (Dis-rel energy density), and cumulative dissipated energy density (cum. Dis-rel energy density) of the shale exhibit distinct stage-dependent characteristics.

At the initial loading stage, the rock mass experiences elastic deformation, and the stress–strain curve is approximately linear. Both the damage factor and the energy dissipation remain at low levels, indicating that the system primarily stores elastic energy. As strain increases, localized stress concentrations induce the initiation of microcracks. The instantaneous dissipated energy density increment begins to show slight fluctuations and gradually increases, while the cumulative dissipated energy density rises slowly, suggesting the onset of intermittent energy dissipation and structural degradation within the rock system.

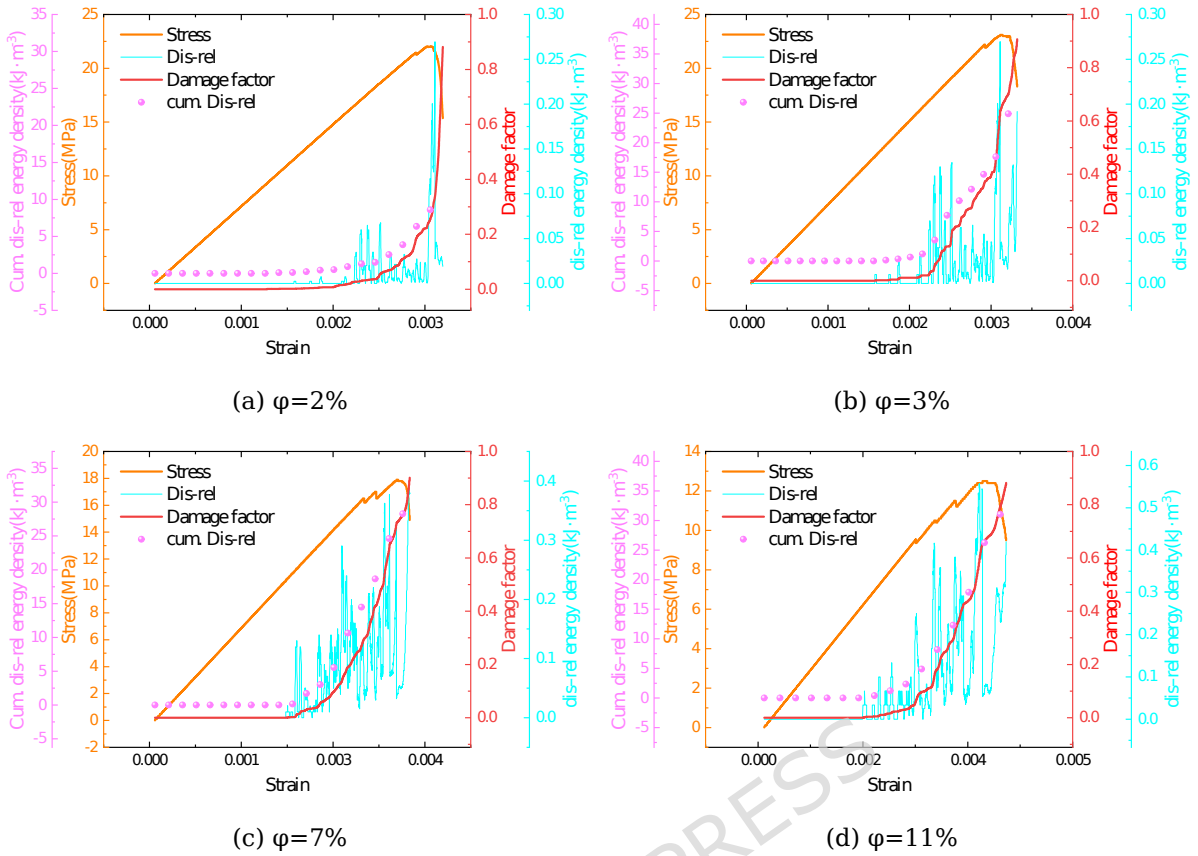

(a) φ=2%　　(b) φ=3%

(c) φ=7%　　(d) φ=11%

Figure.14　Relationship between energy dissipation and damage evolution in digital rocks with different porosities

Upon entering the nonlinear stage, the stress curve develops an inflection point, and the growth rate of the damage factor accelerates with multiple abrupt jumps, corresponding to transient energy release events associated with crack propagation. The sudden rises in the energy release curve correlate closely with the stress drops, highlighting the pulsed nature of energy dissipation during fracture propagation.

When the stress reaches its peak and enters the post-peak stage, the crack network rapidly coalesces and penetrates, leading to a sharp rise in the direct energy release density. The cumulative energy dissipation curve increases steeply, while the damage factor approaches saturation, indicating that the system has transitioned from an energy storage stage to one dominated by energy dissipation. Overall, the evolution of damage exhibits a strong consistency with the energy release process, confirming the validity of the proposed energy-damage coupling relationship within the model.

Pronounced differences are observed among samples with varying porosities. In

low-porosity cores, crack propagation is constrained, leading to relatively gradual energy release and steady damage accumulation. In contrast, high-porosity samples exhibit enhanced pore connectivity, which facilitates cooperative crack propagation. Consequently, distinct energy pulses and abrupt surges in damage appear even during the pre-peak stage, indicating greater brittleness and higher sensitivity to energy perturbations.

5.2 Relationship between shale damage and the multifractal characteristics of fractures-pore structures

As shown in Figure 15, we examine the intrinsic linkage between fracture signals and the multifractal characteristics of pore structures during damage evolution under different porosities. The damage factor is used as the abscissa, and the multifractal metrics—including D_{qmax}, spectral width $\Delta\alpha$, and spectral height difference Δf—are reported for fracture signals (FS) and pore structures (PS).

Overall, D_{qmax} for both FS and PS increases with the damage factor, indicating a progressive increase in structural complexity and heterogeneity as loading proceeds. At early stages, PS already shows appreciable complexity, consistent with the pre-existing multiscale pore architecture. With further damage, FS becomes increasingly active and exhibits larger fluctuations, suggesting that crack growth and coalescence amplify the heterogeneity inherited from the original pore system.

The spectral width $\Delta\alpha$ shows broadly consistent evolution for FS and PS, generally increasing toward the middle-to-late stages. For low-porosity samples (2% and 3%), $\Delta\alpha$ varies mildly, implying comparatively limited restructuring and a more stable damage progression. In contrast, high-porosity samples (7% and 11%) display larger $\Delta\alpha$ increases with more pronounced fluctuations, consistent with more complex and multi-path damage development and stronger pore–fracture reorganization.

For both FS and PS, Δf decreases with increasing damage factor and tends to become negative at later stages, implying a growing contribution of high-magnitude components. High-porosity samples show stronger Δf fluctuations, suggesting a

greater spatial overlap between energy-concentrated zones and rapidly evolving crack–pore regions. Collectively, the synchronous increase in D_{qmax} and $\Delta\alpha$ together with the decline in Δf supports a coupled evolution between fracture development and pore-structure modification, and this coupling becomes more evident with increasing porosity.

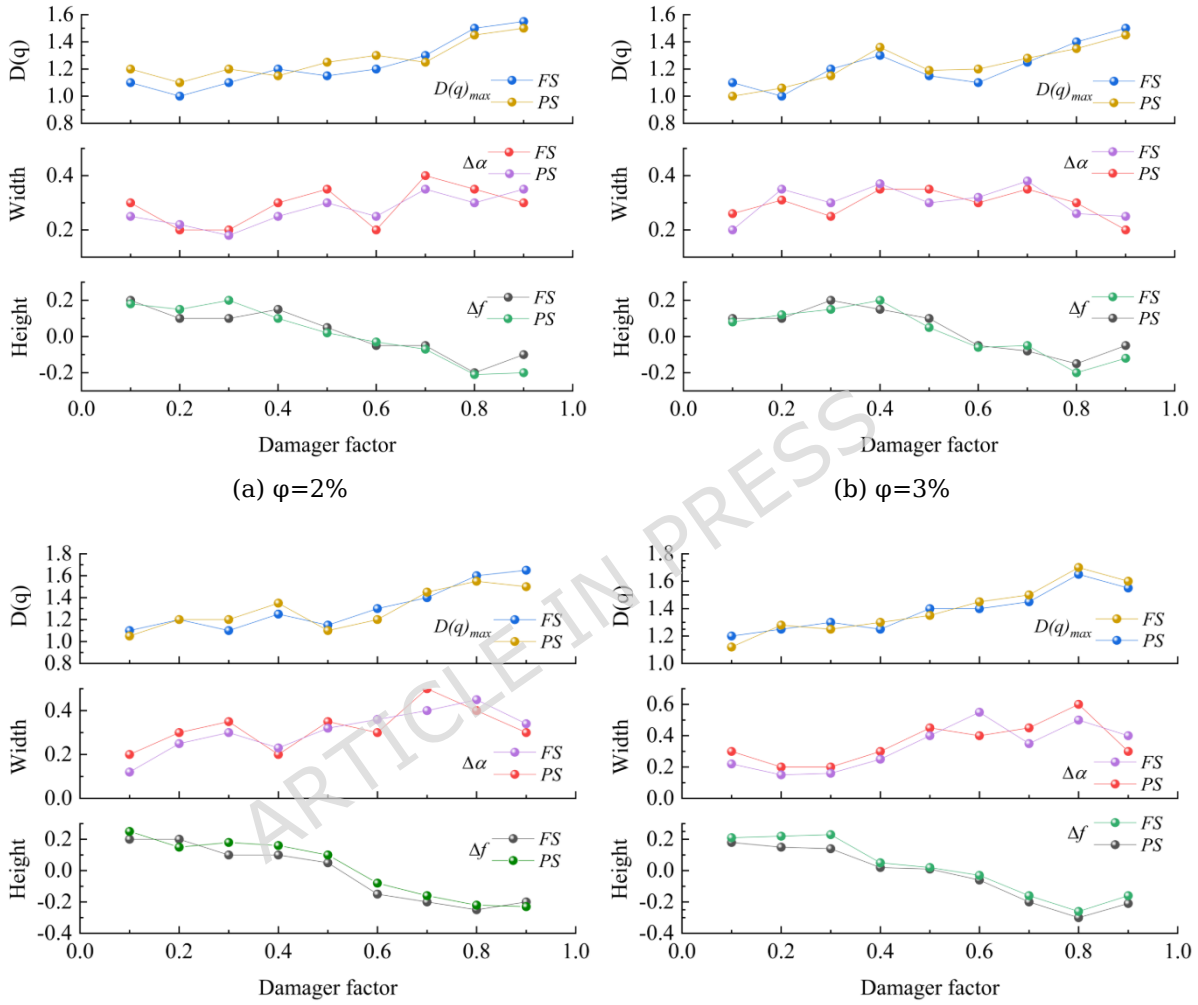

(a) φ=2% (b) φ=3%

(c) φ=7% (d) φ=11%

Figure.15 Multifractal characteristics of damage evolution in digital rocks with different porosities

6. Analysis of shale permeability evolution based on fractal characteristics

Figure 16 summarizes the co-evolution of fracture multifractal characteristics

(FS), pore-structure multifractal characteristics (PS), porosity (φ), and permeability (k) during damage progression in digital shale models with different initial porosities. Overall, variations in the multifractal metrics track the evolution of φ and k, indicating that the progressive reorganization of the pore–fracture network governs flow-related responses.

At the initial loading stage, compaction dominates and pores deform and partially close, resulting in rapid decreases in both φ and k. Fractures are not yet prominent, and the multifractal parameters of FS and PS remain relatively low, consistent with a comparatively uniform internal structure and limited effective flow pathways.

With further loading into the crack-initiation stage, microcracks emerge locally while compaction remains important. The pore structure begins to redistribute, and the multifractal metrics start to fluctuate, reflecting the coexistence of compaction and localized damage. Because fractures are still sparse and poorly connected, the corresponding changes in φ and k remain modest.

Approaching the peak stage, fracture growth intensifies and the multifractal parameters increase markedly, indicating enhanced structural complexity and heterogeneity. Fracture development promotes pore-structure reorganization and improves connectivity, leading to a pronounced increase in φ and more importantly k.

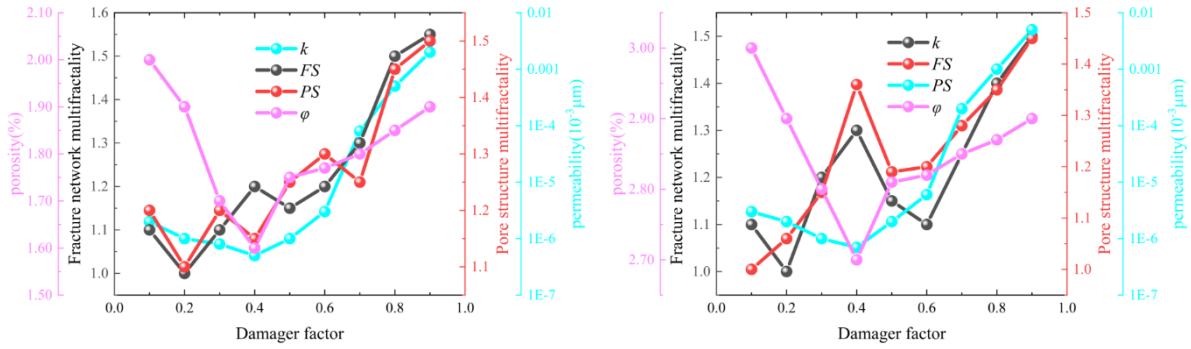

(a) φ=2%

(b) φ=3%

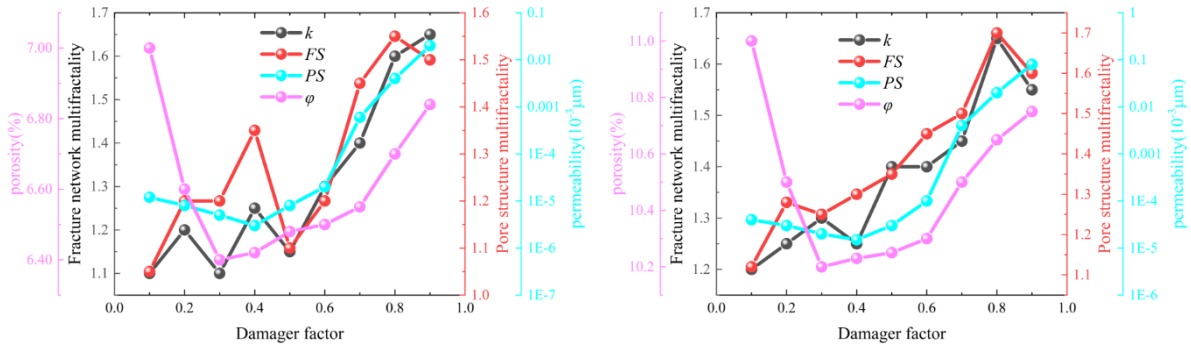

(c) φ=7% (d) φ=11%

Figure.16 Relationship between porosity and permeability and Multifractal characteristics of digital rocks under different porosity conditions

In the post-peak stage, damage becomes pervasive and the pore–fracture system continues to adjust dynamically. The multifractal parameters fluctuate at elevated levels, while φ and k may continue to increase but typically with reduced growth rates, consistent with the progressive opening and subsequent stabilization of dominant flow channels.

Different initial porosities exhibit distinct sensitivities. High-porosity samples facilitate earlier linkage between newly formed fractures and the pre-existing pore network, producing earlier increases in multifractal metrics and a stronger permeability response. Low-porosity samples, in contrast, tend to delay network linkage, leading to a more gradual permeability enhancement.

Overall, the coordinated evolution of multifractal metrics with φ and k supports a continuous transition from compaction-dominated pore closure to damage-driven connectivity enhancement, providing a mechanistic interpretation of permeability evolution during loading-induced damage[36].

7. Discussion

This study investigates the multifractal evolution of fractures and pore structures in shale under uniaxial compression using digital rock reconstruction combined with discrete element simulations. The results demonstrate that the generalized fractal dimension $D_{q_{max}}$, spectral width $\Delta\alpha$, and spectral height difference Δf of both fracture

signals and pore structures evolve systematically with loading, reflecting a progressive increase in structural heterogeneity and spatial complexity.At the early loading stage, fracture activity remains limited and the pore structure is dominated by compaction, corresponding to relatively low multifractal complexity. With fracture initiation and propagation, the multifractal spectrum of fracture signals broadens markedly, accompanied by increasing pore connectivity and heterogeneity. In the post-peak stage, fracture coalescence and pore-network reorganization jointly drive a leftward shift of the spectrum and an expansion of high-energy concentration zones, indicating the onset of global instability.

Compared with previous studies, multifractal analyses have primarily been applied to acoustic emission or electromagnetic radiation signals to characterize fracture activity and energy release during rock failure[22,23]. More recent works have employed CT imaging to reveal the geometric complexity of pore–fracture networks from a static perspective[7,8]. In contrast, the present study integrates multifractal descriptors of fracture signals with pore-structure multifractal characteristics, enabling a quantitative linkage between dynamic fracture evolution and microstructural reorganization.This spatiotemporal dual-scale framework extends conventional fractal approaches by capturing not only the static complexity of pore systems but also their coupled evolution with fracture development under loading. The observed correspondence between multifractal parameters, porosity, and permeability further supports the capability of the proposed approach to characterize damage-driven transport evolution in shale.

Although this study systematically elucidates the coupling relationship between fractures and pore structures through numerical simulation and multifractal analysis, certain limitations should be acknowledged. The finite size of the digital rock samples constrains their ability to capture the global effects of multi-scale fracture networks present in natural rock masses. Moreover, the simulations were conducted under uniaxial compression boundary conditions, without accounting for complex influences such as confining pressure, loading rate, anisotropy, or pore fluid interactions, which may affect deformation and failure behavior under in-situ

conditions. Therefore, caution should be exercised when extrapolating the findings to field-scale applications. In addition, potential uncertainties arising from CT image thresholding and pore extraction may lead to segmentation errors, while the choice of particle size and bonding parameters in the discrete element model could influence the simulated fracture propagation rate and energy release characteristics. Given these factors, the quantitative results presented herein are primarily intended to reveal evolutionary patterns and mechanistic insights rather than provide direct predictions of strength or damage. Future studies should combine experimental observations with larger-scale and multi-condition simulations to further validate and enhance the universality and reliability of the conclusions.

Future research can be further expanded from multi-physics and multi-scale perspectives. On one hand, incorporating triaxial or true-triaxial compression conditions will enable the examination of how confining pressure and loading rate influence the coupled evolution of fractures and pores, thereby providing a more realistic representation of in-situ stress conditions in subsurface reservoirs. On the other hand, advanced high-resolution imaging techniques such as nano-CT and FIB-SEM can be utilized to reconstruct the pore system across scales—from nanopores to microfractures—allowing for a more comprehensive characterization of its fractal features. Meanwhile, coupling multifractal parameters with energy release rate, damage factor, and permeability evolution can facilitate the establishment of unified macro-micro constitutive relationships, revealing the intrinsic coupling mechanisms between energy evolution and structural complexity during shale fracturing. Furthermore, integrating field data from acoustic emission, electromagnetic radiation, and microseismic monitoring with multifractal analyses offers a promising pathway for identifying precursory instability signals, thereby improving the accuracy of stability assessments and hazard predictions in deep shale reservoirs. Collectively, these advancements will enhance our understanding of the multiscale synergistic evolution of fracture-pore systems, extend the application of multifractal theory in rock mechanics and reservoir engineering, and provide a solid scientific basis for ensuring engineering safety and promoting efficient resource development

in complex geological environments.

8. Conclusion

In this study, digital rock reconstruction and DEM simulations were used to quantify the coupled fracture–pore evolution and their multifractal relationship in shale under uniaxial compression. The main conclusions are:

(1) An energy-based damage evolution model was developed, which links stress response to fracture development and reproduces crack initiation, propagation, and coalescence. Samples with higher porosity show more concentrated energy release and more pronounced fracturing, whereas lower-porosity samples exhibit relatively slower damage accumulation.

(2) Fracture signals and pore structures exhibit coordinated multifractal evolution. Pore-structure complexity dominates the multifractal response at the early stage, while fracture growth increasingly governs it after peak stress, and their multifractal parameters show broadly consistent trends across porosity levels.

(3) The multifractal evolution is associated with flow-pathway reorganization. In our simulations, damage-driven fracture growth modifies pore connectivity, leading to a systematic change in porosity and permeability and reflecting the evolution of flow channels.

Overall, multifractal parameters provide effective indicators for characterizing damage stages and structural evolution of the coupled fracture–pore system, offering theoretical support for shale reservoir failure interpretation and stability evaluation.

Funding: This work was supported by the National Natural Science Foundation of China (Grant Nos. 42474156 and 42174143).

Conflict of interest/Competing interests: The authors declare no conflict of interest.

Data availability：The datasets generated and analyzed during the current study are available from the corresponding author upon reasonable request.

Author contribution:

Wang Ziqi: Conceptualization, Methodology, Writing - Original Draft

Sun Jianmeng: Supervision, Funding acquisition, Resources

Wen Haiou: Data curation, Formal analysis, Visualization

Pan Weiliang: Writing - Review & Editing, Project administration

Sun Xiaojun: Data curation, Formal analysis, Visualization

All authors read and approved the final manuscript.

Gao Honglin: Software, Validation, Investigation

References

1.Cai, Q. W. (2024). Three-dimensional fracture propagation model of rock strata fracturing and its application. *China University of Mining and Technology. (in Chinese).*

2.Zhao, Y., Liu, L. Q., Pan, Y. S., et al. (2017). Experimental study on microseismic, charge induction, self-potential, and acoustic emission during rock deformation and fracture. *Chinese Journal of Rock Mechanics and Engineering, 36*(1), 107–123. *(in Chinese).*

3.Wu, J., Tan, J., Xu, J., Li, L., Beroza, G. C., Mumford, K. G., ... & Elsworth, D. (2025). Challenges to sustainable large-scale shale gas development in China. *Proceedings of the National Academy of Sciences*, *122*(18), e2415192122.

4.Zhao, Y., Zhou, H., Zhong, J., et al. (2019). Study on the relation between damage and permeability of sandstone at depth under cyclic loading. *International Journal of Coal Science & Technology, 6*(4), 479–492.

5.Zhao, Z., and Zhou, X. P. (2020). 3D digital analysis of cracking behaviors of rocks through 3D reconstruction model under triaxial compression. *Journal of Engineering Mechanics, 146*(8), 04020084.

6.Zhang, P. S., Hou, J. Q., Zhao, C. Y., et al. (2020). Experimental study on permeability characteristics of red sandstone with different confining pressures and damage degrees. *Chinese Journal of Rock Mechanics and Engineering, 39*(12), 2405–2415. *(in Chinese).*

7.Tang, M., Zhang, T., Li, Y., Hao, Z., Yang, X., Chen, Y., ... & Wang, Y. (2025). Stress-Dependent Microcrack Evolution and Damage Constitutive Model of Low Permeability Sandstone. *Fatigue & Fracture of Engineering Materials & Structures*.

8.Yan, S., Han, L., Zhang, S., Zhao, W., & Meng, L. (2025). Evolution Characteristics of Pore–Fractures and Mechanical Response of Dehydrated Lignite Based on In Situ Computed Tomography (CT) Scanning. Fractal and Fractional, 9(4), 220.

9.Zhu, H. G., Xie, H. P., Yi, C., et al. (2011). CT identification of microcrack evolution in rock materials. *Chinese Journal of Rock Mechanics and Engineering, 30*(6), 1230–1238. *(in Chinese).*

10.Zhao, Y., Qin, W., Jin, A., et al. (2024). Research and analysis of the impact of the pore structure on the mechanical properties and fracture mechanism of sandstone. *Materials Today Communications, 38,* 107753.
11.Wu, J., Wang, Q., Li, Z., et al. (2025). Discrete element modeling for investigating the mechanical behavior of porous granular sea ice specimens under uniaxial compression. *Applied Ocean Research, 162,* 104710.
12.Xiao, N., Chen, J. Q., Qiu, X., et al. (2025). Study on the relationship between porosity and mechanical properties based on rock pore structure reconstruction model. *Applied Sciences, 15*(13), 7247.
13.Rotter, S., Dosta, M., and Düster, A. (2024). Discrete element simulation of the breakage behavior of porous granules utilizing bond models. *Computational Particle Mechanics, 11*(1), 89–103.
14.Baud, P., Wong, T., and Zhu, W. (2014). Effects of porosity and crack density on the compressive strength of rocks. *International Journal of Rock Mechanics and Mining Sciences, 67,* 202–211.
15.Lang, Y. X., Liang, Z. Z., Duan, D., et al. (2019). Reconstruction and parallel simulation of rock mesoscopic pore models based on CT experiments. *Rock and Soil Mechanics, 40*(3), 1204–1212. *(in Chinese).*
16.Cheng, Z. L., Sui, W. B., Ning, Z. F., et al. (2018). Study on microstructural characteristics of digital rock cores and their influence on rock mechanical properties. *Chinese Journal of Rock Mechanics and Engineering, 37*(2), 449–460. *(in Chinese).*
17.Fu, Y., He, Y., and Li, C. (2023). Failure and acoustic emissions of coal–rock combinations with different dip angles in the Shaqu No. 1 Coal Mine. *Advances in Civil Engineering, 2023*(1), 9969802.
18.Zhang, Y., Feng, G., Li, Z., et al. (2024). Acoustic and thermal response characteristics and failure mode of gas-bearing coal–rock composite structure under loading. *Infrared Physics & Technology, 142,* 105517.
19.Klyuchkin, V. N., Novikov, V. A., Okunev, V. I., et al. (2022). Acoustic and electromagnetic emissions of rocks: insight from laboratory tests at press and shear machines. *Environmental Earth Sciences, 81*(3), 64.
20.Mingyang, S., Quangui, L., Qianting, H., et al. (2024). Evolution and correlation of acoustic emission and resistance parameters during coal fracture propagation. *Natural Resources Research, 33*(5), 2135–2154.
21.Yin, S., Song, D., He, X., et al. (2022). Structural health monitoring of building rock based on stress drop and acoustic–electric energy release. *Structural Control and Health Monitoring, 29*(2), e2875.
22.Niu, Y., Liu, G. J., Hu, Y. J., Xu, K., & Wang, Y. W. (2026). Mechanical Responses and Temporal Multifractal Behaviors of Rock–Coal–Rock Composite Body under Uniaxial Compression Using an AE Monitoring Tool. *International Journal of Geomechanics*, *26*(1), 04025302.
23.Liu, J., Li, Q., Wang, X., et al. (2022). Dynamic multifractal characteristics of acoustic emission from composite coal–rock samples with different strength rocks. *Chaos, Solitons & Fractals, 164,* 112725.
24.Gu, Y., Wu, X., Jiang, Y., Guan, Q., Dong, D., & Zhuang, H. (2025). Evolution of

Pore Structure and Fractal Characteristics in Transitional Shale Reservoirs: Case Study of Shanxi Formation, Eastern Ordos Basin. *Fractal and Fractional*, *9*(6), 335.
25.Li, J., Liu, C., Liu, H. M., et al. (2022). Study on meso-damage mechanism of shale reservoir rocks based on digital core models. *Chinese Journal of Rock Mechanics and Engineering, 41*(6), 1103–1113. *(in Chinese).*
26.Liu, G., Fang, Z., Zhang, Z., Liu, H., Lv, R., Wang, X., ... & Barakos, G. (2024). Improved Strategy for Multifractal Characterization of CO2 Adsorption in Micropores. *Energy & Fuels*, *38*(21), 20449-20461.
27.Gao, M., Yang, M., Lu, Y., He, P., & Zhu, H. (2024). Mechanical characterization of uniaxial compression associated with lamination angles in shale. *Advances in Geo-Energy Research*, *13*(1).
28.Feng, K., Liu, G., Zhang, Z., Liu, H., Lv, R., Wang, X., ... & Barakos, G. (2025). Multifractal Characterization of Methane Adsorption in Coal Pores. *Langmuir*.
29.Liu, G., Fang, Z., Zhang, Z., Liu, H., Lv, R., Wang, X., ... & Barakos, G. (2024). Improved Strategy for Multifractal Characterization of CO2 Adsorption in Micropores. *Energy & Fuels*, *38*(21), 20449-20461.
30.Halsey, T. C., Jensen, M. H., Kadanoff, L. P., Procaccia, I., & Shraiman, B. I. (1986). Fractal measures and their singularities: The characterization of strange sets. *Physical review A*, *33*(2), 1141.
31.Xie, J., Gao, M. Z., Zhang, S., et al. (2021). Experimental study on triaxial fracture behavior and energy release law of deep coal under the effect of loading rates. *Journal of Central South University (Science and Technology), 52,* 2713–2724.
32.Liu, X. H., Xue, Y., Zheng, Y., et al. (2021). Study on energy release during coal–rock fragmentation process under impact loading. *Chinese Journal of Rock Mechanics and Engineering, 40*(S2), 3201–3211. *(in Chinese)*
33.Gong, F. Q., Yan, J. Y., and Li, X. B. (2018). Criterion for rockburst tendency based on linear energy storage law and residual elastic energy index. *Chinese Journal of Rock Mechanics and Engineering, 37*(9), 1993–2014. *(in Chinese).*
34.Kachanov, M. (1992). Effective elastic properties of cracked solids: critical review of some basic concepts. *Applied Mechanics Reviews, 45*(8), 304–335.
35.Yang, Y. J., Wang, D. C., Guo, M. F., et al. (2014). Study on rock damage characteristics based on triaxial compression acoustic emission tests. *Chinese Journal of Rock Mechanics and Engineering, 33*(1), 98–104. *(in Chinese).*
36.Li, F., Elsworth, D., Feng, X. T., Chen, T., Zhao, J., Li, Y., ... & Cui, G. (2025). Revisiting the normal stiffness–permeability relations for shale fractures under true triaxial stress. *Journal of Rock Mechanics and Geotechnical Engineering*.